A planar rod model with flexible cross-section for the folding and the dynamic deployment of tape springs: improvements and comparisons with experiments

Elia Picault, Pernelle Marone-Hitz, Stéphane Bourgeois, Bruno Cochelin, François Guinot

A planar rod model with flexible cross-section for the folding and the dynamic deployment of tape springs: Improvements and comparisons with experiments

E. Picault [b], P. Marone-Hitz [a], S. Bourgeois [a,⇑], B. Cochelin [a], F. Guinot [c]

[a] LMA, Centrale Marseille, CNRS, UPR 7051, Aix-Marseille Univ, F-13451 Marseille Cedex 20, France
[b] LMA, CNRS, UPR 7051, Aix-Marseille Univ, Centrale Marseille, F-13402 Marseille Cedex 20, France
[c] Thales Alenia Space, F-06156 Cannes La Bocca Cedex, France

Keywords:
Non-linear elastic rods Tape spring, Folding Dynamics

A planar rod model with flexible cross-section has been recently proposed in literature (Guinot et al., 2012). This model is especially suitable for the modeling of tape springs, which develop localized folds due to the flattening of the cross-section. Starting from a complete non-linear elastic shell model, original kinematics assumptions (inspired from the elastica model) have been made to describe the important in-plane changes of the cross-section shape. In the present work, the choice of the position of the rod reference line is discussed. This choice plays an important role in the overall behavior because of the large changes of the cross-section shape. We show that the model published in Guinot et al. (2012) can be improved by considering the centerline as the rod reference line. This enhanced model is then validated through quantitative comparisons with experimental results of dynamic deployments taken from literature.

1. Introduction

In its free state, a tape spring can be considered as a straight thin-walled beam with an open circular cross-section of constant transverse curvature. One of the most studied test (Seffen and Pellegrino, 1999) illustrating its behavior is the bending test shown in Fig. 1. Under applied bending rotations at the ends, this structure behaves at first like a beam before the sudden appearance of a localized fold, indicating snap-through buckling. This fold is created by a localized flattening of the cross-section which drastically reduces the moment of inertia and concentrates the bending deformation in the fold area. We shall note that away from the fold, the tape spring remains almost straight and undeformed. Playing with a carpenter's tape measure, one can easily experience the formation of one or several folds, the motion of a fold along the tape, the splitting of a single fold into two or the merging of two folds into one.

Tape springs offer a wide range of compact folded or coiled configurations and thus are an interesting alternative to articulated rigid structures with hinges and bolts for the design of deployment systems. However, since their behavior is sensitive to instabilities and can exhibit a sudden loss of stiffness with largely deformed shapes, the modeling of such structures is a challenging issue.

As mentioned in Guinot et al. (2012), the natural approach for the modeling of tape springs consists in the full computation of a non-linear shell model in the framework of large displacements, large rotations and dynamics (Hoffait et al., 2009; Seffen et al., 2000; Walker and Aglietti, 2007). This approach leads to hard-to-drive and time consuming simulations but provides accurate static and dynamic solutions for any loading configurations and boundary conditions. The difficulties reside mainly in the slenderness of the structure combined with the transverse curvature that lead to a highly flexible structure. The slenderness and the transverse curvature also make the structure sensitive to localized buckling that occurs when overall bending leads to compression effects on the edges of the cross-section.

Considering the particular shape of a tape spring, one can think about an intermediate model based on a thin-walled beam model. The literature is extremely extensive on this topic, from the pioneering work of Vlassov (1962) to the recent developments on the Generalized Beam Theory (Dinis et al., 2009;Silvestre, 2007;

⇑ Corresponding author. Tel.: +33 491054412.
E-mail addresses: picault@lma.cnrs-mrs.fr (E. Picault), pernelle.marone-hitz@centrale-marseille.fr (P. Marone-Hitz), stephane.bourgeois@centrale-marseille.fr (S. Bourgeois), bruno.cochelin@centrale-marseille.fr (B. Cochelin), francois.guinot@thalesaleniaspace.com (F. Guinot).

Fig. 1. Folding of a tape spring.

Silvestre et al., 2011;Gonçalves and Camotim, 2009) introduced by Schardt (1994). Compared to all these models, the main originality of the rod model proposed in Guinot et al. (2012) lies in the taking into account of the high flexibility of the cross-section in its plane through a suitable kinematics inspired from the elastica theory (Euler, 1744; Goss, 2009), which leads to a reduced number of kinematic parameters. Starting from a non-linear shell model, the main idea underlying the model consists in a parametrization of the cross-section shape (and not of the relative displacements) under the inextensibility assumption of the 'cross-section curve'. This approach has been applied to the folding and dynamic deployment of tape springs in the previous work (Guinot et al., 2012) with a rod model involving only four kinematic parameters. It has been shown that it qualitatively handles the creation of folds, the motion of a fold along the tape and the splitting of a single fold into two. It has however been mentioned that this model has some difficulties to account for snap back phenomena during unloading (see Remark 5 in Guinot et al. (2012)). In the present work, some assumptions on the kinematics are discussed and a new proposal is made to improve the model. It is shown that the choice of the rod reference line is important when large relative displacements in the cross-section are considered. A new proposal is investigated and validated on the classical example treated in Seffen and Pellegrino (1999) and Guinot et al. (2012): the creation of a fold under a pure bending moment prescribed by opposite rotations at ends. The improved model, for which the rod line is taken as the centerline, is able to account for the snap back phenomenon for this example. This improved model is then validated by quantitative comparisons with dynamic deployment experiments presented in Seffen and Pellegrino (1999).

In the following, Section 2 begins to recall the foundations of the model presented in the previous work (Guinot et al., 2012), i.e. the basic assumptions about the kinematics that allow to reduce the shell model to a rod one. The choice of the rod reference line is discussed and the case in which the rod line is taken as the centerline is developed. The strain and kinetic energies of the rod model are then obtained. The Hamilton Principle is used to implement the model in the finite element software COMSOL Multiphysics (2011) that performs an automatic differentiation of the energies to obtain the weak formulation of the problem. The next sections are devoted to numerical examples.

In Section 3, a tape spring submitted to opposite cross-section rotations at ends is studied. The overall response (moment versus prescribed rotations at ends) is compared for the previous model, the proposed new model and the shell model. The results show that, contrary to the previous model, the proposed model is able to capture the snap back during the unloading of the prescribed rotations. This result is confirmed by a path-following approach that allows the computation of the whole equilibrium paths, which are consistent with the critical angles at which the snap-through occur for the two rod models. The fold properties are also compared for the shell model and the proposed new model.

In Section 4, the dynamic deployment of a folded tape spring is considered. The improved model is applied to the experiments presented in the work of Seffen and Pellegrino (1999) and quantitative comparisons are analyzed.

2. The rod model

2.1. Kinematic description and basic assumptions

A tape spring is regarded as a shell that can be assimilated to a rod with a thin-walled cross-section. In the initial configuration, the middle surface of the shell is supposed to result from the extrusion of a circular cross-section curve along a straight rod line, as shown in Fig. 2. More precisely, we construct a fixed orthonormal frame $(O;e_1;e_2;e_3)$ such that the initial middle surface results from the extrusion along e_1 of an arc of circle contained in the plane $(O;e_2;e_3)$. The line defined by $(O;e_3)$ is chosen to be the axis of symmetry of the arc in the plane $(O;e_2;e_3)$ with O an arbitrary point on this axis of symmetry. The initial middle surface of the tape is then symmetric with respect to the plane $(O;e_1;e_3)$ by construction of the fixed orthonormal frame $(O;e_1;e_2;e_3)$. The axis $(O;e_1)$ is chosen to be the rod reference line in the initial configuration.

We naturally introduce a curvilinear coordinate system $(s_1;s_2) \in [0;L] \times [-a;a]$ to map the geometry of the tape, with L the initial length of the tape and 2a the initial length of the cross-section curve[1]. The material line defined by $s_1 \in [0;L]$ and $s_2 = 0$ is called the 'bottom line' (see Fig. 2).

At time t, in the deformed configuration, the position of a material point M on the middle surface is given by:

$$OM(s_1;s_2;t) = OG(s_1;t) + GM(s_1;s_2;t); \quad (1)$$

where OG is the position vector in the deformed configuration of the point which is the intersection of the rod line and the cross-section plane in the undeformed configuration.

The rod model kinematics presented in Guinot et al. (2012) relies on four assumptions:

(i) the cross-section curve remains in a plane after deformation,
(ii) the cross-section plane is orthogonal to the tangent vector of the rod line in the deformed configuration,
(iii) the shape of the tape which is initially symmetric with respect to the plane $(O;e_1;e_3)$ remains symmetric with respect to this plane,
(iv) the cross-section curve is considered inextensible and remains circular.

The two first assumptions are the classical hypotheses used in the Euler–Bernoulli beam theory. The symmetry assumption (iii) then involves that the motion of the rod line is restrained to the plane $(O;e_1;e_3)$: the displacement of a point G on the rod line is given by the two components $u_1(s_1;t)$ and $u_3(s_1;t)$ and the rotation

[1] The initial length of the cross section curve was set to a in the previous work (Guinot et al., 2012). It is here set to 2a to obtain more concise expressions in the following.

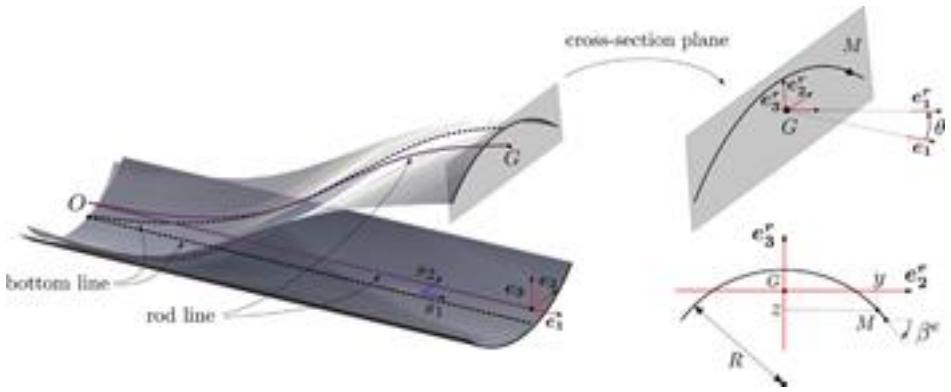

Fig. 2. Geometric and kinematic description of the tape spring (left) and its cross-section (right), with $(O; e_1; e_2; e_3)$ the fixed orthonormal frame and $(G; e^r_1; e^r_2; e^r_3)$ the rotated frame that follows the cross-section plane.

of the cross-section plane $\theta(s_1; t)$ is around the axis e_2. We introduce the rotated frame $(G; e^r_1; e^r_2; e^r_3)$, following the cross-section plane, in which the coordinates of the material point M are denoted by $y(s_1; s_2; t)$ and $z(s_1; s_2; t)$. We then obtain:

$$\overrightarrow{OG} = u_1(s_1; t)\, e_1 + u_3(s_1; t)\, e_3,$$
$$\overrightarrow{GM} = y(s_1; s_2; t)\, e_2 + z(s_1; s_2; t)\, e^r_3. \quad (2)$$

According to assumption (ii), the rotation θ and the displacements u_1 and u_3 are not independent. The orthogonality between the tangent vector of the rod line and the cross-section plane leads to:

$$\begin{cases} \overrightarrow{OG}_{;1} = (1 + u_{1;1})\, e_1 + u_{3;1}\, e_3, \\ \overrightarrow{OG}_{;1} \cdot e^r_3 = 0 \text{ with } \overrightarrow{OG}_{;1} = \left\| \overrightarrow{OG}_{;1} \right\| e^r_1 \end{cases}$$

where $X_{;i}$ stands for the partial derivative of X with respect to s_i. The last Eq. (3) can be rewritten in the form of the following constraint:

$$C(u_1; u_3; \theta) = \sin\theta\,(1 + u_{1;1}) + \cos\theta\, u_{3;1} = 0. \quad (4)$$

The inextensibility assumption (iv) of the cross-section curve is inspired by the elastica theory (Euler, 1744; Goss, 2009). This theory handles large elastic deflections of rods and is naturally adapted to take into account the high flexibility of the cross-section curve. A crucial advantage of this theory resides in the fact that the planar motion of the cross-section curve can be described by a single kinematic parameter: the angle $\beta(s_1; s_2; t)$ between the tangent to the cross-section curve and the vector e^r_2 (see Fig. 2). The local coordinates of a point in the cross-section are then given by:

$$y_{;2} = \cos\beta \quad \text{and} \quad z_{;2} = \sin\beta. \quad (5)$$

When making this assumption, we suppose that the most important effect governing the changes in the cross-section shape is the adjustment of the overall bending inertia (the second moment of area of the cross-section) of the rod in order to minimize its elastic energy: the flattening of the cross-section concentrates the overall bending deformation and leads to the formation of localized folds. In doing so we suppose that transverse strains can be neglected to evaluate the overall bending inertia and that the inextensibility assumption is enough to describe the overall shape of the cross-section curve.

Moreover, we suppose that the cross-section curve remains circular (assumption (iv)). Therefore the angle β is a linear function of s_2:

$$\beta(s_1; s_2; t) = \frac{s_2}{a}\, b^e(s_1; t); \quad (6)$$

where $b^e(s_1; t) = \beta(s_1; s_2 = a; t)$ is said to be the opening angle of the cross-section. The initial value of the opening angle of the cross-section is denoted by b^e_0. Explicit expressions of the local coordinates y and z can be easily derived from the integration of Eq. (5):

$$y(s_1; s_2; t) = \int_0^{s_2} \cos\beta(s_1; n; t)\, dn = \frac{a}{b^e} \sin\frac{b^e s_2}{a};$$
$$z(s_1; s_2; t) = \int_0^{s_2} \sin\beta(s_1; n; t)\, dn = \frac{a}{b^e}\left(1 - \cos\frac{b^e s_2}{a}\right). \quad (7)$$

The constants of integration $y(s_1; s_2 = 0; t)$ and $z(s_1; s_2 = 0; t)$ specify the position of the rod line with respect to the bottom line (see Fig. 2). The symmetry assumption (iii) leads to: $y(s_1; s_2 = 0; t) = 0$. However, the position of the bottom line in the z-direction is still not fixed. In the previous work (Guinot et al., 2012), the bottom line is chosen as the rod line, which yields: $z(s_1; s_2 = 0; t) = 0$. Another choice consists in defining the rod line as the centerline, i.e. the curve which passes through the centroids of the cross-sections, and the condition $\int_a z\, ds_2 = 0$ is written to obtain $z(s_1; s_2 = 0; t)$. If the rod line is taken as the centerline, we then have:

$$y(s_1; s_2; t) = \frac{a}{b^e} \sin\frac{b^e s_2}{a};$$
$$z(s_1; s_2; t) = \frac{a}{b^e}\left(\sin\beta(b^e) - \frac{b^e}{a}\cos\frac{b^e s_2}{a}\right). \quad (8)$$

These two possibilities (rod line = bottom line or rod line = centerline) are equivalent in the case of non-deformable cross-section: they lead to the same kinematics described by two different sets of parameters. It corresponds to the classical introduction of an offset of the centerline in a beam model. But when the cross-section highly deforms in a non-uniform way along the rod, these two choices lead to two different kinematics as illustrated in Fig. 3 in the case of the folding of tape spring: the orthogonality condition of the cross-section plane with respect to the rod line leads to different ways of describing the deformation. This question has not been studied in the previous work and it will be shown in this paper that the choice of the centerline as the rod line is a better option than the bottom line.

Finally, whatever the choice for the rod line is, the kinematics of the tape spring is described by only four parameters attached to the rod line (functions of the time t and the initial abscissa s_1 of the cross-section along the rod):

- the translations u_1 and u_3 of the points on the rod line,
- the rotation θ of the cross-section plane around e_2,
- and the opening angle b^e characterizing the shape of the cross-section.

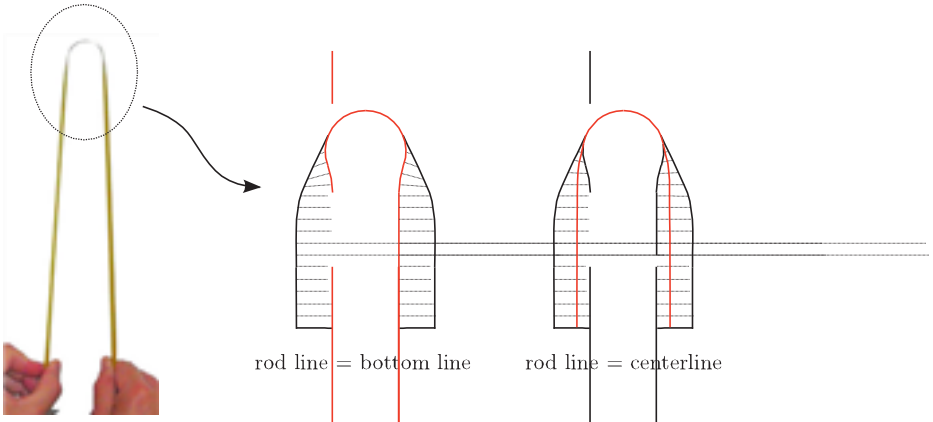

Fig. 3. Schematic folding of a tape spring with two straight and undeformed parts, a circular zone where the cross section is completely flattened, and two transition zones. The cross section planes are represented in dashed black lines and the rod lines are in red solid lines. In the transition zones, the two choices for the reference line (bottom line or centerline) do not lead to the same kinematics when the orthogonality of the cross-section plane with respect to the rod line is considered.

The approach presented herein for a simple cross-section shape kinematics may be generalized to more complex shapes or kinematics by choosing a suitable discretization (e.g. Ritz, FE, etc.) of the angle $\beta(s_1; s_2; t)$ with respect to the transverse coordinate s_2 and by adding some kinematic parameters (Guinot et al., 2012).

In the following, the model presented in Guinot et al. (2012) is rewritten with the rod line taken as the centerline.

2.2. Strains measures and strain energy

The tape spring is first considered as a thin shell undergoing membrane and bending strains e_{ab} and k_{ab} defined respectively by the Green–Lagrange measure and the difference between the initial and actual curvature tensors. The tape spring is submitted to large displacements but the membrane strains remain small in practice: since the thickness is very small compared to the two other dimensions a and L of the shell, local and global buckling will prevent large strains to occur. As shown in Guinot et al. (2012), the small membrane strains assumption leads to the following simplified expressions (the choice of the rod line does not impact on these expressions):

$$\begin{cases} e_{11} = e^r + z k^r + e^s; \\ k_{11} = \dot{\beta} k^r \cos\beta + k^s_{11}; \\ k^{22} = k^{s22}; \\ k^{12} = k^{s12}; \end{cases} \quad \text{with} \quad \begin{cases} e^r = u_{1;1} + \frac{1}{2}\left(u^2_{1;1} + u^2_{3;1}\right); \\ k^r = h_{;1}; \\ e^s = \frac{1}{2} y^2_{;1} + z^2_{;1}; \\ k_{s11} = z_{;11}\cos\beta + \dot{\beta} y_{;11}\sin\beta; \\ k_{s22} = b_{;2} + \dot{\beta} b_{0;2}; \\ k_{s12} = b_{;1}; \end{cases} \tag{9}$$

where b_0 is the value of the angle β in the undeformed initial configuration. These Eqs. (9) enlighten the strains induced by the global rod kinematics (variables with the superscript r) and those induced by the deformation of the cross-section curve (superscript s). We recognize in e^r and k^r the classical expressions of the usual tensile strain and the bending curvature of a rod in the framework of large displacements and large rotations. We can notice that the strains e^s and k^s_{ab} only depend on the angle β and vanish if the cross-section remains undeformed. The strains e_{ab} and k_{ab} are associated with the membrane stresses and bending moments N_{ab} and M_{ab} in the strain energy. Since the shell width is small compared to the tape spring length ($a/L \ll 1$), we suppose that $N_{22} = N_{12} = 0$ according to classical beam theory assumptions and the elastic strain energy is written:

$$U_e = \int_0^L \int_{-a}^{a} \frac{1}{2}\left(e_{11} N_{11} + k_{ab} M_{ab}\right) ds_2\, ds_1. \tag{10}$$

Moreover, the shell is considered elastic and isotropic. The constitutive equations are then expressed by:

$$N_{11} = A e_{11} \quad \text{and} \quad \begin{cases} M_{11} = D_{11} k_{11} + D_{12} k_{22}; \\ M_{22} = D_{12} k_{11} + D_{22} k_{22}; \\ M_{12} = D_{33}(2 k_{12}); \end{cases} \tag{11}$$

with

$$A = Eh; \quad D_{11} = D_{22} = \frac{Eh^3}{12(1-\nu^2)}; \quad D_{12} = \nu D_{11}; \quad D_{33} = \frac{Eh^3}{24(1+\nu)} = D_{11}\frac{(1-\nu)}{2} \tag{12}$$

where h is the shell thickness and E and ν are respectively the Young's modulus and the Poisson's ratio.

Using the constitutive Eqs. (11) and the expressions (9) for the strains, the elastic strain energy (10) can be written, after integration over the cross-section as:

$$U_e = \int_0^L \left(u^r_e + u^s_e + u^{rs}_e\right) ds_1; \tag{13}$$

in which $u^r_e; u^s_e$ and u^{rs}_e are the three terms that define the strain energy density of the rod model:

$$\begin{cases} u^r_e = \frac{1}{2}\left(2Aa(e^r)^2 + A z^2 + D_{11}\overline{\cos^2\beta}\,\dot{\beta}^2\right)\dot{k}^{r\,2}; \\ u^s_e = \frac{1}{2}A(e^s)^2 + D_{11}\dot{k}^2_{11s} + D_{22}\dot{k}^2_{22s} \\ \quad + 2D_{12}\dot{k}_{s11}\dot{k}_{s22} + 4D_{33}\dot{k}^2_{s12}; \\ u^{rs}_e = Ae^r e^s + Ak^r z e^s + \dot{k}^r D_{11}\overline{\cos\beta k^s_1} + D_{12}\overline{\cos\beta k^s_2}; \end{cases} \tag{14}$$

where the overline denotes an integration over s_2: $\overline{X(s_1)} = \int_{-a}^{a} X(s_1; s_2)\, ds_2$. The first term u^r_e corresponds to the classical strain energy of a rod. The second term u^s_e only depends on the variable β and represents the strain energy due to the variation of the cross-section shape, independently of the overall rod behavior. The last term u^{rs}_e induces a coupling between the overall rod behavior and the deformation of the cross-section. Expressions of the energies are formally the same than those obtained for the bottom line model presented in Guinot et al. (2012), but the expressions of integrals, given in Appendix A, are different. For example, there is no more coupling between axial stretching and bending in u^r_e for the centerline model because $z = 0$.

2.3. Kinetic energy

Starting from the kinetic energy of the initial shell model in which the rotation inertia is neglected and introducing the chosen kinematics, we find the following expression for the kinetic energy of the rod model:

$$U_k(u_1, u_3, h, b) = \int_0^L \ddot{y}\, u_k^r + u_k^s \, ds_1,$$

$$\text{with} \quad \begin{cases} u_k^r = \frac{1}{2}\left(a\,\ddot{u}_2 + u_2\right) + q\,h\,z_2\,\dot{h}^2, \\ u_k^s = \frac{1}{2}\, q\, h\, \left(y_2^2 + z_2^2\right); \end{cases} \qquad (15)$$

where q is the material density and the notation $\dot{X}$ stands for the time derivative of X. We recognize in u_k^r the classical kinetic energy of a rod with non deformable cross-section, with a translational part and a rotational part. The term u_k^s comes from the deformability of the cross-section. Notice that the coupling term u_k^{rs} that appears in the bottom line model vanishes in the case of the centerline model.

2.4. Work of external forces and kinematic boundary conditions

The work of external distributed forces is introduced in an overall way. In the numerical examples presented later on, a generalized force density with components denoted by f_1 and f_3 will be considered, leading to the following expression of the external work:

$$W_{ext} = \int_0^L (f_1\, u_1 + f_3\, u_3)\, ds_1 \qquad (16)$$

The boundary conditions that can be imposed on the end sections of the tape spring are directly derived from strains expressions (9) with respect to the kinematic parameters of the rod model:

- the translations u_1 and u_3 of the points on the rod line,
- the rotation h of the cross-section,
- the angle b^e that characterizes the shape of the cross-section,
- the first derivative $b^e_{,1}$ of this angle that prescribes the local rotation at each point of the cross-section (clamped end section for example),

The expression (16) only takes into account the distributed loads and should be completed by the contribution of the concentrated loads applied on the end sections and in duality with u_1, u_3, h, b^e and $b^e_{,1}$ if necessary.

2.5. Numerical implementation

Starting from the energies, the equations of motions can be obtained thanks to the Hamilton Principle which requires the calculus of variation of the following functional:

$$H(u_1, u_3, h, b^e, k) = \int_{t_1}^{t_2} (U_k - \ddot{y}\, U_e + W_{ext} + W_C)\, dt; \qquad (17)$$

with

$$W_C(u_1, u_3, h, k) = \int_0^L k\, C\, ds_1; \qquad (18)$$

where $k(s_1, t)$ is a Lagrange multiplier associated with the constraint $C = 0$ (see Eq. (4)) that ensures the orthogonality between the cross-section plane and the rod line. For the numerical simulations, the finite element software COMSOL Multiphysics (2011) has been used because it offers the possibility to handle directly the expressions of the energies by proceeding to an automatic differentiation. Only the kinetic energy U_k requires an explicit calculus of variation. Indeed, for the kinetic energy and contrary to the other terms U_e, W_{ext} and W_C in (17), an integration by parts with respect to time is necessary to obtain the weak formulation. As in the previous work (Guinot et al., 2012), the expressions (A.3) in appendix have been replaced by their Taylor series around $b^e = 0$ (considering the first four non-zero terms) to face with numerical singularities. It should also be mentioned that in dynamic simulations, only the translational part in the term u_k^r is taken into account and the term u_k^s is neglected in the kinetic energy density (see (15)).

For all the following results, the rod line is meshed with Hermite quintic finite elements and the default implicit time-dependent solver of COMSOL (BDF solver) is used with a variable time-step and a numerical damping handled automatically (highly non-linear option).

3. Static folding: bottom line versus centerline

We return to the first example treated in Guinot et al. (2012): the creation of a fold under a pure bending moment prescribed by opposite rotations at ends. The moment-rotation relationship is well documented in literature and Fig. 4 shows the schematic response according to the work of Seffen and Pellegrino (1999). This response is not symmetric with respect to the origin and the two senses of bending have to be distinguished: opposite-sense bending when $M\,h > 0$ and equal-sense bending when $M\,h < 0$ (see Fig. 4). For small prescribed rotations at ends, the tape spring behaves like a classical beam and the response exhibits a linear part. In opposite-sense bending, the response then becomes non-linear and a maximum value of moment is reached before a snap through caused by the sudden appearance of a fold. After the creation of this fold, the moment stays quite constant with respect to the prescribed angle h. This moment denoted M_p is called the fold-propagation moment in opposite-sense bending. When the rotation is brought back to zero, the path is not the same and a jump back to the initial linear part of the curve occurs for a smaller angle than the one observed for the creation of the fold: the fold disappears at a smaller angle than the one it appears. In equal-sense bending, the linear part ends sooner and there is a bifurcation without snap through. This bifurcation coincides with the appearance of a flexural–torsional deformation mode that disappears after the creation of the fold (Seffen and Pellegrino, 1999). As in the case of opposite-sense bending, the moment remains rather constant with respect to the prescribed angle h after the creation of the fold. When the rotation is brought back to zero, the response follows the same path.

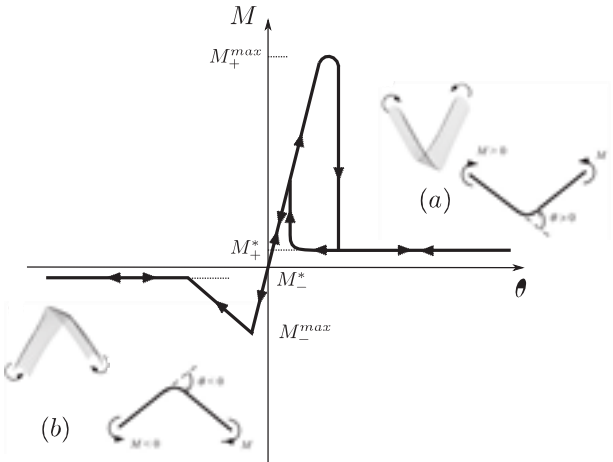

Fig. 4. Schematic response of a tape spring submitted to opposite rotations at ends: bending moment vs prescribed rotation (according to Seffen and Pellegrino (1999)), in opposite-sense bending (a) and equal-sense bending (b).

Notice that the equal-sense bending can not be correctly treated with the proposed planar rod model because the out-of-plane behavior and especially twisting is not taken into account. A 3D rod model with flexible cross-section including twisting and warping effects will be proposed in a forthcoming work. Only the opposite-sense bending is considered in the following. In the previous work in which the bottom line is taken as the rod line, it has been mentioned that the model has some difficulties to account for the jump back when the angle is brought back to zero. We will show that the model that uses the centerline as the rod line accounts better for the jump back.

In the following, the example treated in Guinot et al. (2012) is revisited. The material and geometric properties are recalled in Table 1. The boundary conditions are given by:

at the first end section ($s_1 = 0$): $u_1 = u_3 = 0$; $h = \dot{y} h_L$; $b^e = b^e_0$ and $b^e_{,1}$ free;
at the second end section ($s_1 = L$): u_1 free, $u_3 = 0$; $h = h_L$; $b^e = b^e_0$ and $b^e_{,1}$ free.

Fig. 5 shows the results obtained for the moment-rotation relationships for a loading step up to a prescribed rotation $h_L = 0.16$ rad, followed by an unloading step back to zero. The blue curve (b) is relative to the model that uses the bottom line as the rod line. The red curve (c) is relative to the model that uses the centerline as the rod line. The result obtained with a shell model by using a pseudo-arclength continuation method in Abaqus (2012) is recalled from Guinot et al. (2012). On the right in Fig. 5, several deformed shapes are presented at significant prescribed rotations. These deformed shapes are reconstructed with the results of $u_1(s_1)$; $u_3(s_1)$; $h(s_1)$ and $b^e(s_1)$ obtained with the 1D rod models. The superimposed color plots are those of the angle b and illustrate the curvature of the cross-section curve. Fig. 6 offers a more detailed analysis of these deformed shapes with the plots of $b^e(s_1)$ and $h(s_1)$.

Table 1
Geometrical and material properties of the tape spring for the static folding test.

Length L (m)	Half width a (mm)	Thickness h (mm)	Opening angle b^e_0 (rad)	Young's modulus E (MPa)	Poisson's ratio ν
1.17	30	0.15	0.6	210,000	0.3

During the loading step, the moment-rotation relationships obtained with the two models (centerline and bottom line) are quite similar. The scenario obtained with the centerline model described here is the same as the one obtained with the bottom line model described in Guinot et al. (2012): at first, the tape behaves as a classical beam with a non deformable cross-section and a linear moment-rotation relationship. The two models give exactly the same response in this linear part: this is in accordance with the above mentioned result that for a non deformable cross-section, the two models are equivalent. This relationship rapidly becomes non-linear, due to the flattening of the cross-section. At the beginning, this flattening varies smoothly all along the tape and is maximum in the middle (see the plots of $b^e(s_1)$ for the deformed shapes 2 and 3 in Fig. 6). This non-uniform flattening leads to a non-uniform bending inertia and the rotation of the cross-section is no more linear with respect to s_1 (see the plots of $h(s_1)$ for the deformed shapes 2 and 3 in Fig. 6). The creation of the fold is then due to the localization of the flattening in the middle of the tape (see the plot $b^e(s_1)$ for the deformed shape 4). The tape recovers its undeformed shape outside the fold region where the cross-section is completely flattened (see the plots of $h(s_1)$ and $b^e(s_1)$ for the deformed shape 4). Before the creation of the fold, the peak moment obtained with the centerline model is slightly lower than the one obtained with the bottom line model. In the same way, the critical rotation at which the fold occurs is also lower and is more in accordance with the one obtained with a finite element shell model in Abaqus.

The most significant difference between the two models is observed during the unloading step. Contrary to the centerline

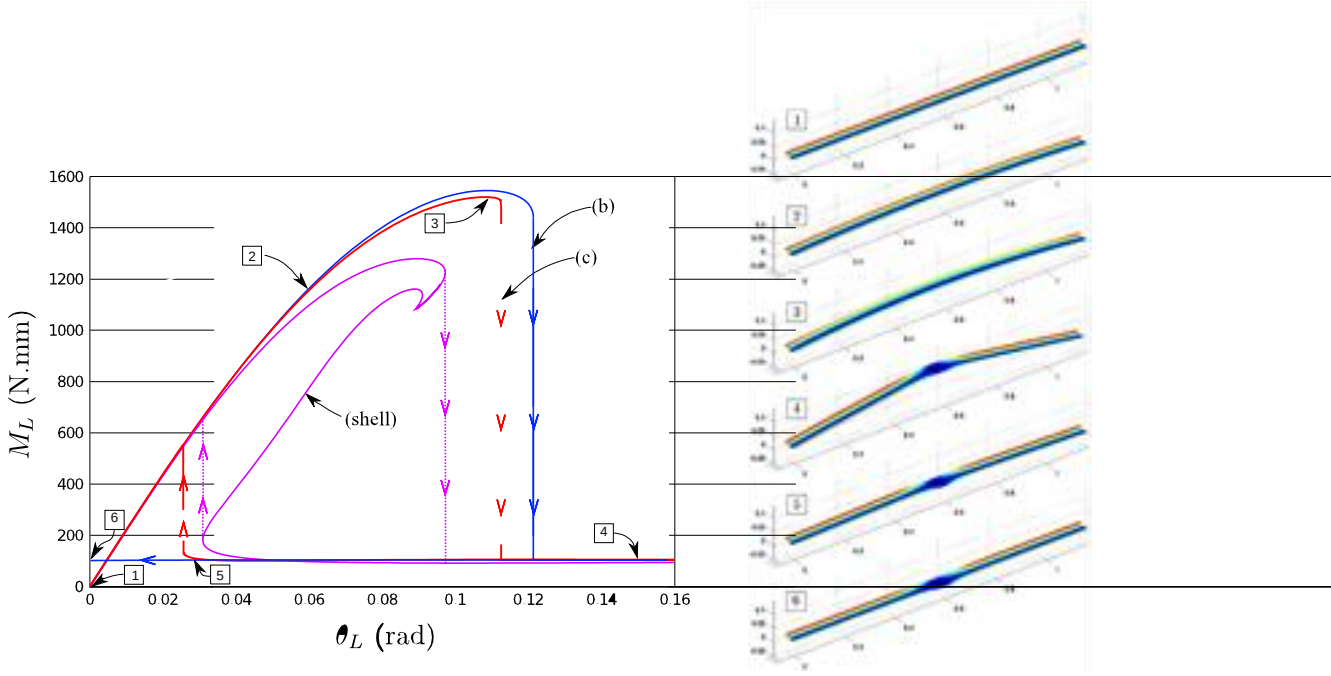

Fig. 5. On the left: moment-rotation relationships obtained with the bottom line model (b) and the centerline model (c) and comparison with the one obtained with a shell model by using a pseudo-arclength continuation method in Abaqus. On the right: deformed shapes at six significant imposed rotations h_L obtained with the extended rod models. Superimposed color plots of $b(s_1; s_2)$. First deformed shape: initial free state at $h_L = 0$ rad. The deformed shapes 2 to 5 are relative to the centerline model, corresponding respectively to $h_L = 0.06$, 0.11 and 0.15 rad during the loading step and $h_L = 0.03$ rad during the unloading step. The deformed shape 6 is relative to the bottom line model and is obtained after complete unloading at $h_L = 0$ rad.

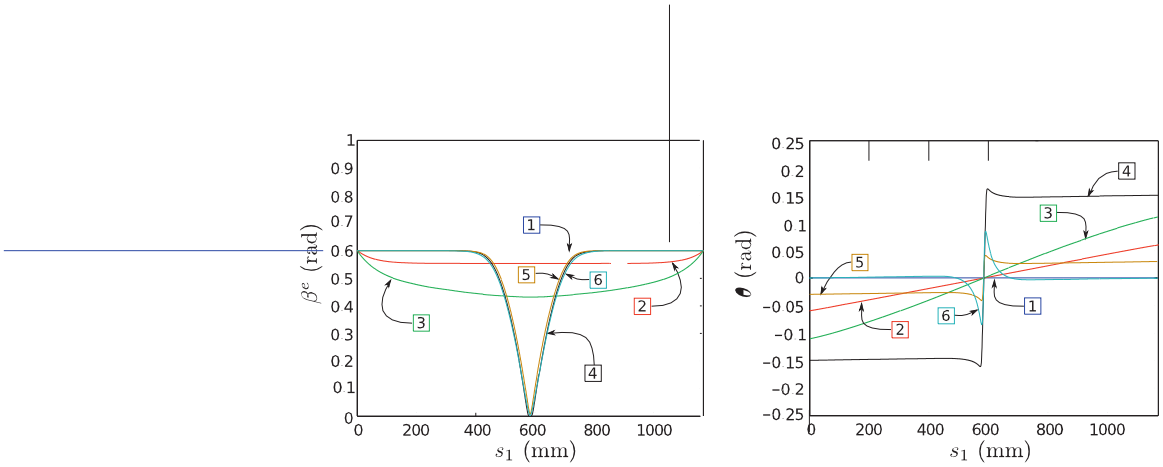

Fig. 6. Opening angle $b^e(s_1)$ and rotation $h(s_1)$ of the cross-section along the rod for the six deformed shapes shown in Fig. 5.

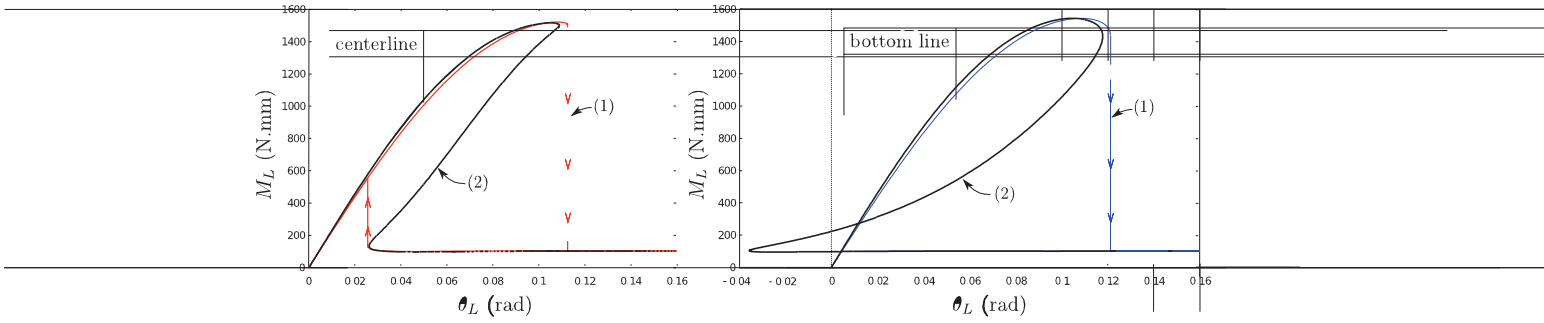

Fig. 7. Moment-rotation relationships obtained with a time-dependent solver (1) and a pseudo-arclength continuation (2) for the centerline model (left) and the bottom line model (right). The equilibrium paths (2) are in accordance with the results (1) obtained with the time dependent solver and are fully consistent with the observed jumps. They also confirm that contrary to the centerline model, the bottom-line model is unable to account for the snap-back during the unloading when cross-section rotations are prescribed at the ends of the tape spring.

model, the bottom line model is unable to account for the jump back. With the bottom line model, the fold persists up to zero applied rotation [2] (see the deformed shape 6 in Fig. 5). The plots of $h(s_1)$ and $b^e(s_1)$ associated to the deformed shape 6 in this figure suggest that the kinematic assumptions made for the bottom line model introduce artificial internal forces that allow an unrealistic equilibrium configuration at zero applied rotation, for which there is a fold in the middle of the tape and two slightly bent regions on either side. The deformed shape 5 in Fig. 5 and associated plots on Fig. 6 illustrates the state of the tape spring just before the jump back according to the centerline model. The fold persists up to the jump back during which it disappears.

This result is confirmed by the computation of the equilibrium paths (see Fig. 7) obtained for the rod models using a pseudo-arclength continuation (Cochelin et al., 2007). An orthogonal collocation method with piecewise polynomial interpolations is used for the discretization of the strong formulations associated to the stationary condition of the potential energy given by Eqs. (13), (14) and (16). For the sake of simplicity, expressions of energies are rewritten under the assumptions of moderate cross-section rotations and small opening angles b^e. The numerical developments have been made in the software package MANLAB (Karkar et al., 2010) and Fig. 7 shows that the obtained equilibrium paths are in accordance with the results obtained with a time-dependent solver (BDF solver in Comsol) in which the loading consists of increments of the cross-section rotations at ends h_L (the small differences can be explained by the additional assumptions made to simplify the strong formulations associated to the rod models). The jumps obtained with the time-dependent solver are consistent with the equilibrium paths obtained with the pseudo-arclength continuation. For the bottom-line model, the equilibrium path explains that there is no snap-back during the unloading when cross-section rotations are prescribed at the ends of the tape spring.

The centerline model clearly performs better than the bottom line model with respect to the scenario described in literature and especially with the schematic response Fig. 4 explained in the work of Seffen and Pellegrino (1999). These results can also be compared to the reference ones obtained in Guinot et al. (2012) with the finite element software Abaqus using shell elements. It shows that the centerline model is able to predict the peak moment and the critical rotations at which the jumps occurs within 20%.

Fig. 8 offers a more detailed description of the fold properties after snap-through has taken place ($h_L = 1{:}5$ rad). The results obtained with the shell model (Abaqus) are compared to those obtained with the centerline model. The deformed shapes at the top of the figure show that the two models lead to the same overall results. The left bottom plot in Fig. 8 offers a detailed comparison of the normalized total height of the cross-section along the tape in the deformed configuration. For the centerline rod model, $Dz = z(s_1; s_2 = a) + \ddot{y}\, z(s_1; s_2 = 0)$ with $z(s_1; s_2)$ given by Eq. (8) and Dz_0 is the initial total height (when $b^e = b^e_0$). For the shell model, the value of Dz is taken as

$$Dz = \sqrt{\ddot{y}\,Du_1^{\ddot{y}2} + Dz_0 + Du_3}^{\,2};$$

with $Du_i^s = u_i^s(s_1; s_2 = a) + \ddot{y}\, u_i^s(s_1; s_2 = 0)$ and $u_i^s(s_1; s_2)$ the displacements of the shell middle surface. When Dz/Dz_0 equals one, the cross-section is undeformed and a value of zero corresponds to a completely flattened cross-section. The plots of Dz/Dz_0 show that the rod model is in good agreement with the shell model as regards the extent of the fold (region where the cross-section is completely flattened) and the extent of the transition regions on either side (regions where the cross-section passes from an undeformed shape to a completely flattened configuration). Notice that

[2] In the previous work (Guinot et al., 2012), the response for unloading exhibits some unexplained partial jumps back. It is due to some numerical problems that have been solved here with a more rigorous control of the calculation.

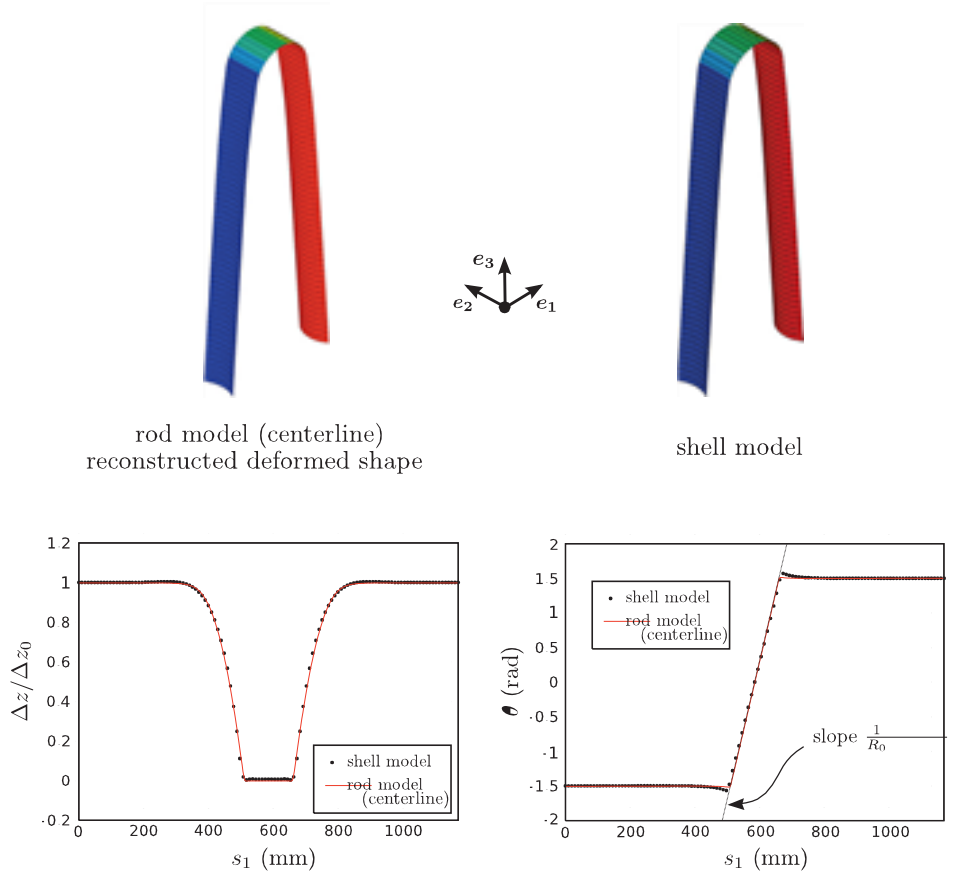

Fig. 8. Deformed shapes and detailed description of the fold properties for a prescribed rotation at ends h_L = 1.5 rad: centerline rod model versus shell model. On the top left, reconstructed deformed shape obtained with the centerline rod model (superimposed color plots of the cross-section rotation). On the top right, deformed shape obtained with the shell model (superimposed color plots of the rotation around e_2 of the normal to the middle surface). On the bottom left, normalized total height of the cross-section along the tape in the deformed configuration for the two models. On the bottom right, comparison of the cross-section rotation along the centerline (rod model) and the rotation (around e_2) of the normal to the middle surface along the bottom line of the tape (shell model).

$Dz=Dz_0$ does not strictly equal zero for the shell model in the fold region. Seffen and Pellegrino (1999) have already mentioned that the cross-section is not completely flat across this region: small bulges appear on the edges. For the centerline rod model, the transverse curvature is assumed to be uniform in the cross-section and a very small value is found for b^e. The right bottom plot in Fig. 8 offers a comparison between the cross-section rotation along the centerline (rod model) and the rotation (around e_2) of the normal to the middle surface along the bottom line of the tape (shell model), in the deformed configuration. The rod model is once again in good agreement with the shell model. The two regions where the rotation is constant correspond to the straight undeformed parts of the tape. In the fold region, considering that the cross-section is completely flattened, the linear part indicates that the deformed shape is cylindrical with a uniform longitudinal curvature equal to the initial transverse curvature $\frac{1}{R_0} = \frac{b^e}{a}$. These detailed comparisons show that the centerline rod model is able to account quite accurately for the geometrical characteristics of the fold region and the transition areas. This model is used for the simulations of the dynamic deployments presented in the following.

4. Dynamic deployments: comparison with experiments from literature

4.1. Introduction

The numerical simulations are based on the deployment experiments presented in Seffen and Pellegrino (1999). Three tests are considered (see Fig. 9). All three springs are initially folded with a single fold of ca. 1.57 rad in the middle. Then one of the end section is released while the other is held fully clamped. The main difference between the three configurations is the orientation of gravity.

It must be recalled that the geometry of the tape springs is different for the three tests, as shown in Table 2.

The elastic properties of the constitutive material are not directly given in the paper of Seffen and Pellegrino (1999). They have been identified by using the values of the fold-propagation moments that are given for the tape springs used in the three configurations. The authors propose simplified expressions for the fold-propagation moments M_{θ} et M_{ψ} (see Fig. 4 for the significance of these moments):

$$M_{\theta} = 2b^e D; \qquad M_{\psi} = \psi 2b^e D \quad \text{with} \quad D = \frac{Eh^3}{12(1-\nu^2)} \tag{19}$$

Using these expressions (19), a Young's Modulus and a Poisson's ratio can be identified for each test. We adopted for our

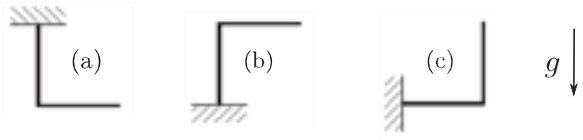

Fig. 9. The three folded initial configurations for the deployment experiments.

Table 2
Geometrical properties of the tape springs.

Test	Length L (mm)	Half width a (mm)	Thickness h (mm)	Initial opening angle β_0^e (rad)
(a)	515	16.946	0.1	1.145
(b)	505	13.63	0.1	0.94
(c)	516	16.82	0.1	1.16

simulations the mean values that are reported in Table 3. They are consistent with the elastic properties found in literature for the constitutive material of the tape springs used for the tests (Beryllium Copper alloy). For the density, we adopted a mean value found in literature for this kind of alloy.

The simulations are performed in three steps:

step 1: static folding without gravity (kinetic energy $U_k = 0$ during this step),
step 2: introduction of the gravity (in statics),
step 3: dynamic deployment by releasing the boundary conditions at one end.

The tape is fully clamped at the end section $s_1 = 0$ in all steps: $u_1 = u_3 = \eta = 0$; $\beta^e = \beta_0^e$. At the other end $s_1 = L$, the boundary conditions depend on the step. During the first step, the displacements u_1 and u_3 are free, the rotation η is increased from zero to a maximum value η_f and the opening angle is maintained: $\beta^e = \beta_0^e$. In the second step, the displacements u_1 and u_3, the rotation η, and the opening angle β^e are fixed and the gravity is applied with an orientation that depends on the test (see Fig. 9). At the beginning of the last step, the displacements, the rotation and the opening angle are instantaneously released and the resulting motion is studied.

All the folding steps are carried out in opposite-sense bending. The moment-rotation relationships are similar to those presented Fig. 5 obtained in the previous section. The fold propagation moments in opposite-sense bending $M_{\bar{p}}$ obtained with the center line model are very close to those of Seffen and Pellegrino (1999): the simulations lead to 33.7, 27.7 and 34.2 N mm for the tests (a), (b) and (c) respectively and the values from experiments given in Seffen and Pellegrino (1999) are 33.9, 27.8 and 34.1 N mm respectively.

4.2. Results for the deployment tests

We first focus on test (b). Fig. 10 shows the evolution of the rod line during the deployment step, obtained with the proposed centerline model. The predicted scenario, characterized by the traveling of the fold along the tape, is in agreement with the experimental results of Seffen and Pellegrino (1999). At first, the fold moves down (until 0.10 s) while the straight free part of the tape grows and rotates counterclockwise. Then the fold rebounds when it reaches the bottom. Since the bottom end is clamped, the flattening cannot move to the end of the tape and the opening flexibility of the cross-section acts as a spring effect to bounce the fold. The fold moves up and down three other times, while the free straight part of the tape oscillates in rotation around a position which becomes increasingly vertical. When the free part passes through the vertical position, the fold disappears and the tape behaves as a classical beam in overall bending, with oscillations that resemble the first free-vibration bending mode of a cantilever beam.

Table 3
Material properties of the tape springs.

Young's modulus E	Poisson's ratio ν	Density ρ
128,000 MPa	0.276	8,350 kg m^{-3}

According to these observations, Seffen and Pellegrino (1999) have proposed to model the tape spring with two straight bars of variable length, joined together by an angular spring that accounts for the fold area. The kinematics can then be described with only two parameters: the fold angle η between the clamped straight part and the free straight part and the non-dimensionalized length κ of the free straight part (see Fig. 11). The angular spring is assumed to be massless and the kinematics of the straight parts is described by rigid body motions. Two approaches are considered to derive the equations of motion: an energy formulation and an impulse-momentum formulation. Fig. 11 shows the experimental results and the results obtained by Seffen and Pellegrino with the impulse-momentum formulation for test (b). This formulation is more suitable than the energy formulation to account for the loss of energy during the reflection of the fold at the end clamped cross-section. The left plots show the results obtained with the proposed model when no viscous damping is introduced. These results are in agreement with both the experiments and the model of Seffen and Pellegrino during the first moving down of the fold, but we observe differences after the first reflection. In particular, some oscillations appear just after the first reflection, due to bending deformation modes. In the model of Seffen and Pellegrino and for the experimental results, the free straight part is assumed to be perfectly straight but our model predicts some bending effects due to the sudden stop of the traveling fold. In Fig. 11, the plot of η corresponds to the value of the rotation $\eta(L)$ at the end cross-section and does not result from an averaging over the assumed free straight part. These bending effects are illustrated in Fig. 12 that shows the deformed shapes of the spring and the evolutions of the rotation $\eta(s_1)$ and the opening angle $\beta^e(s_1)$ along the rod at some significant time values. The first free deformed shapes (from 1 to 3) illustrate the moving down of the fold. The plots of $\eta(s_1)$ and $\beta^e(s_1)$ clearly show the traveling of the fold area (where $\beta^e(s_1) = 0$ and $\eta(s_1)$ is not constant) from the middle $s_1 = L/2$ to the bottom $s_1 = 0$ of the spring. The fourth deformed shape illustrates the bending effect that occurs in the free folded part of the spring which is assumed to remain straight in the work of Seffen and Pellegrino: the rotation $\eta(s_1)$ is not constant in this part. Some oscillations are present in the curve $\beta^e(s_1)$ at this time value. They are induced by localized buckling effects (wave modes localized on lateral edges along the tape) due to compression that occurs at the edges of the cross-section because the spring is submitted to equal-sense bending. The deformed shape 4 clearly shows that the folded part of the spring undergoes equal-sense bending and that the cross-section shape oscillates along the rod (see the superimposed color plots). The last deformed shape 5 illustrates the move up of the fold after the reflection.

The left plot in Fig. 11 shows that the dissipation that occurs in the clamped end during the reflection plays an important role. A simple way to account for this phenomenon is to introduce viscous damping terms that involve the more increasingly constrained kinematic parameters when the fold approaches the base. Following this idea, we introduce in the model the viscous dissipation density

$$D = \frac{1}{2}\gamma(\dot{\beta}^e(s_1))^2; \qquad (20)$$

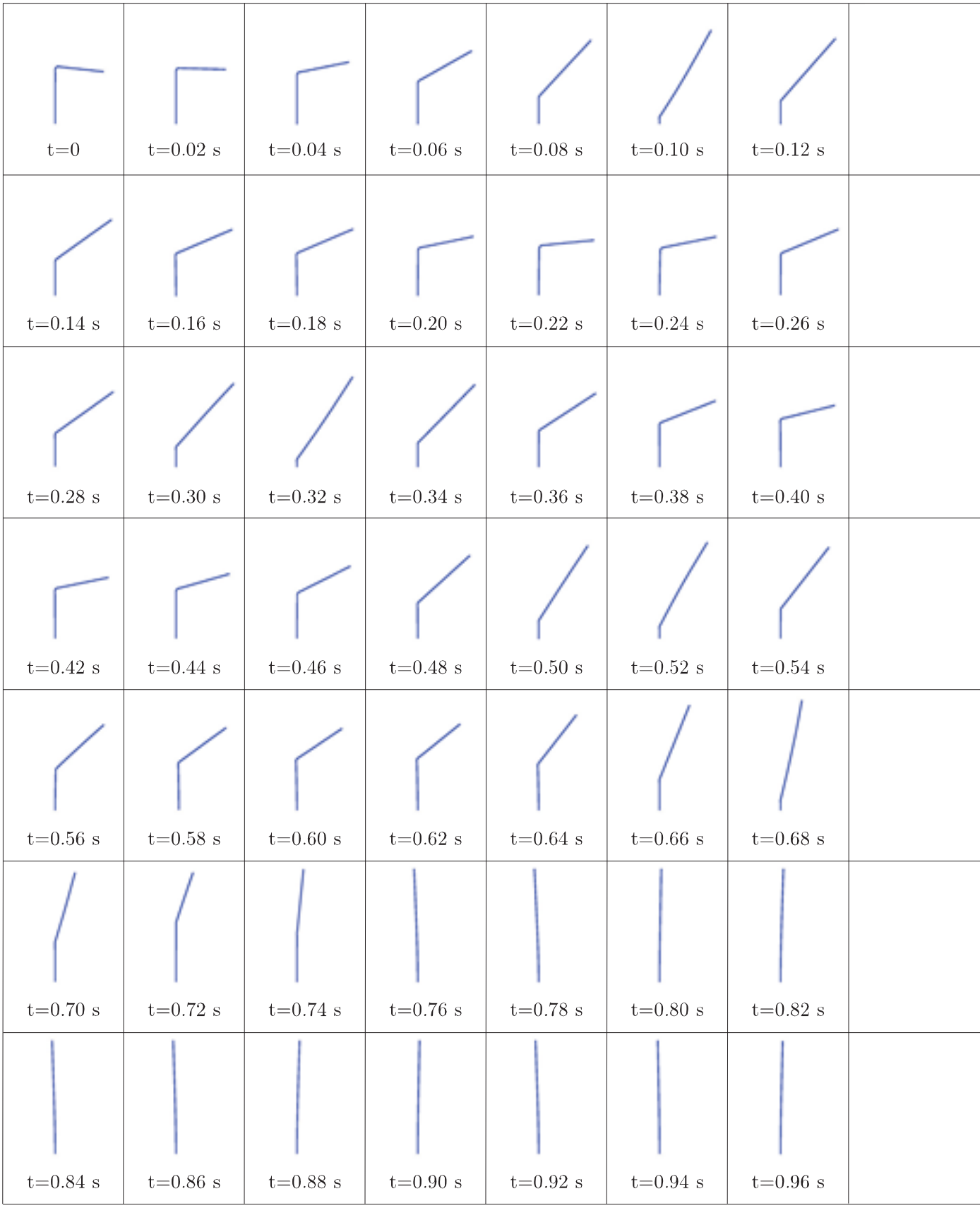

Fig. 10. Deformed shape of the rod line during the deployment step for test (b). It shows the traveling of the fold along the tape spring between the middle and the bottom of the tape with a rebound phenomenon at the bottom. The fold disappears after the fourth rebound and the tape then behaves as a beam which oscillates according to the first free-vibration bending mode.

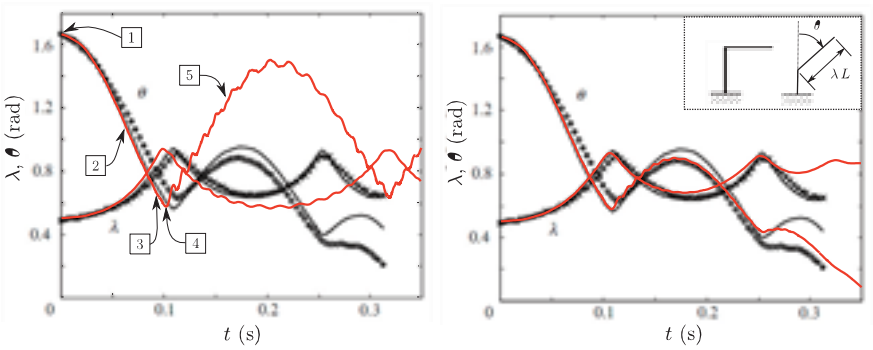

Fig. 11. Results obtained for test (b). Evolution of the fold angle h and the non-dimensionalized length k of the free straight part of the spring with respect to time. Crosses 1 and circles
: experiments. Thin black solid lines: impulse-momentum discrete model from Seffen and Pellegrino (1999). Thick red solid lines: proposed model, without viscous damping (left) and with viscous damping (right). (For interpretation of the references to color in this figure legend, the reader is referred to the web version of this article.)

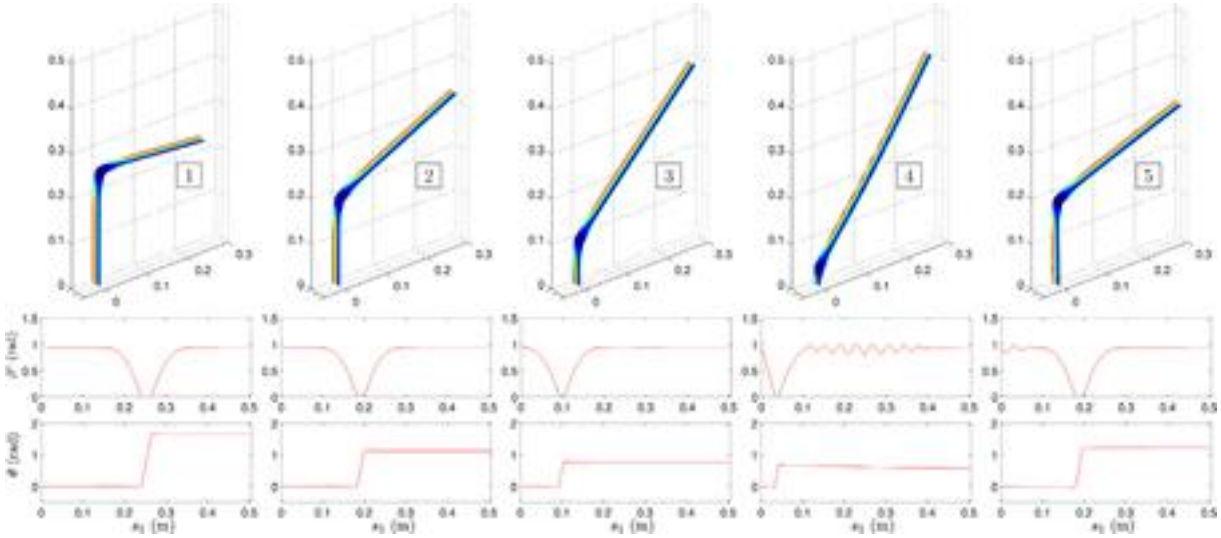

Fig. 12. Reconstructed deformed shapes of the tape at five significant time values during the deployment step for test (b), with superimposed color plots of angle b. From 1 to 5: t=0, 0.06, 0.085, 0.102 and 0.16 s. Bottom plots: opening angle b°ðs1Þ and rotation hðs1Þ of the cross-section plane along the rod for the five deformed shapes.

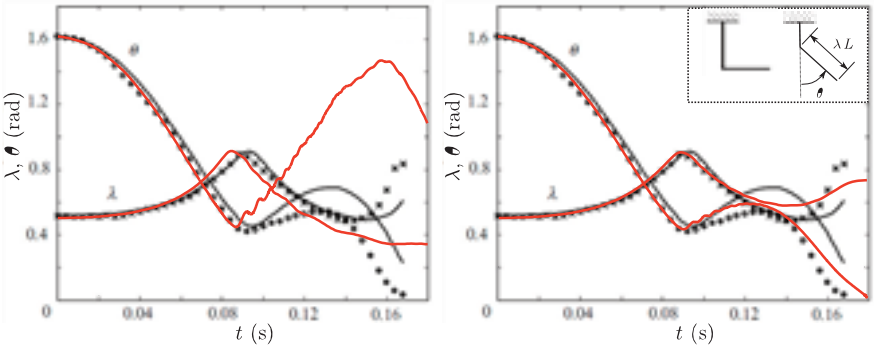

Fig. 13. Results obtained for test (a). Evolution of the fold angle h and the non-dimensionalized length k of the free straight part of the spring with respect to time. Crosses 1 and circles
: experiments. Thin black solid lines: impulse-momentum discrete model from Seffen and Pellegrino (1999). Thick red solid lines: proposed model, without viscous damping (left) and with viscous damping (right). (For interpretation of the references to color in this figure legend, the reader is referred to the web version of this article.)

that involves the opening angle b^e and a single viscous parameter g that must be identified with experiments. The results obtained with this damping model (with g = 6 1 10$^{\ddot{y}4}$ N s) are shown in the right plots of Fig. 11. It should be noticed that the dissipation introduced in the model does not modify the response during the first moving down of the fold but has a significant effect on the response after the reflection. The introduction of the viscosity clearly improves the results when compared to experimental results.

The results obtained for the tests (a) and (c) are shown in Figs. 13 and 14 respectively. The viscous parameter is taken as g = 7 1 10$^{\ddot{y}4}$ N s for both tests. The comparisons between the model and the experiments are as conclusive as in the case of test (b).

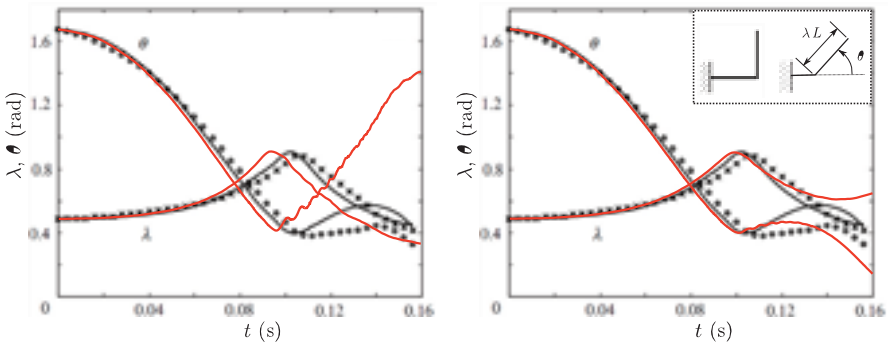

Fig. 14. Results obtained for test (c). Evolution of the fold angle h and the non-dimensionalized length k of the free straight part of the spring with respect to time. Crosses 1 and circles
: experiments. Thin black solid lines: impulse-momentum discrete model from Seffen and Pellegrino (1999). Thick red solid lines: proposed model, without viscous damping (left) and with viscous damping (right). (For interpretation of the references to color in this figure legend, the reader is referred to the web version of this article.)

5. Conclusion

A planar rod model with highly flexible cross-section has been recently proposed in literature for the modeling of tape springs. Starting from a non-linear shell theory, the main idea underlying the model, inspired from the elastica theory, consists in a parametrization of the cross-section shape under the inextensibility assumption of the 'cross-section curve'. It has been shown that this 1D rod model, involving only four kinematic parameters, is able to reflect a wide range of phenomena: creation of folds, migration of a fold along the tape, splitting of a single fold into two. It has however been mentioned that the model has some difficulties to account for some snap back phenomena. In the present work, the model has been improved by discussing the choice of the position of the rod reference line. Contrary to the case of a classical beam model with a nearly rigid cross-section, this choice is of great importance when large relative displacements in the cross-section are encountered. It has been shown in this work that the choice of the centerline is a better choice than the one used in the previous works. The improved model has been validated by comparison with numerical reference results obtained for a classical test: the creation of a fold under a pure bending moment prescribed by opposite rotations at ends. It has also been validated by comparison with experiments results of dynamic deployments taken from literature.

The proposed approach is an alternative to shell models that are hard-to-drive and time consuming: it is a rod model with only four kinematic parameters. It is rich enough to account for the creation, the traveling or the disappearance of folds. The generalization of the model to 3D motion should allow to treat more complex folding, coiling and deployment scenarios by including the possibility of twisting.

Acknowledgments

The work presented in this paper was supported by doctoral Grants from region PACA, CNRS, and Thales Alenia Space.

Appendix A. Characteristic functions for a circular cross-section

The angle b is set to:

$$b = b^e \frac{s_2}{a} \qquad (A.1)$$

From this expression, the integrals over the section, introduced in the energies (14) and (15) can be easily derived:

$$\begin{cases} z^2 = a^3 I_{z^2}; \\ \overline{\cos^2}(b) = a I_{c^2}; \\ \bar{e}^{s^2} = a^5 I_{\quad} \left(b^e_{,1}\right)^4; \\ \bar{k}_{11}^{s^2} = a^3 \left(I_{k^{04}} \left(b^e_{,1}\right)^4 + I_{k^{02}k^{00}} \left(b^e_{,1}\right)^2 b^e_{,11} + I_{k^{00}2} \left(b^e_{,11}\right)^2\right); \\ \bar{k}_{22}^{s^2} = \frac{2}{a}\left(b^e - \ddot{y}\right)^2; \\ \overline{\left(\frac{s}{s}\right)}\left(k_{11}^{s} k_{22}^{s} = a\left(I_{k^{02}} b_{,1}^{e\,2} + I_{k^{00}} b_{,11}^{e} \ddot{y} b^e - \ddot{y} b_0^e\right)\right); \\ \bar{k}_{12}^{s^2} = \frac{2a}{3}\left(b^e_{,1}\right)^2; \\ e^s = a^3 I_{d^{02}} \left(b^e_{,1}\right)^2; \\ \overline{\left(z e_e^s = \tfrac{1}{2} a^4 I_{ze} b_{,1}\right)}; \\ \overline{\cos}(b) k_{11}^{s} = a^2 \left(I_{ck^{02}} b_{,1}^{e\,2} + I_{ck^{00}} b_{,11}^{e}\right); \\ \overline{\cos}(b) k_{22}^{s} = I_c \ddot{y} b^e; \\ \left(\overline{z^2} = \tfrac{2}{3} a^3 I_{d^{02}} b^e\right)_0^2 \end{cases} \qquad (A.2)$$

where the geometrical functions I only depend on the angle b^e and characterize the shape of the section:

$$\begin{cases} I_{z^2}(b^e) = \frac{2b^{e2}(b^e \sin(2b^e) + 2\cos(2b^e) - 2)}{2b^{e4}}; \\ I_{c^2}(b^e) = \frac{b^e + \sin(b^e)\cos(b^e)}{b^e}; \\ I_{d^{04}}(b^e) = \frac{24b^{e8}\ddot{y}b_0^{e6}(2\cos(2b^e) + b^e(1 + 2b^{e5}(1060\sin(2b^e) - 30\sin(4b^e))}{240b^{e12}} \\ \quad + \frac{5b^{e4}(632\cos(2b^e) - 51\cos(4b^e)) + b^{e6}(67 + b^{e3}(915\sin(4b^e) - 5130\sin(2b^e)))}{240b^{e12}} \\ \quad + \frac{240b^{e2}\sin^2(b^e)\ddot{y}(29\cos(2b^e) + b^e(13920 + b^e\sin^3(b^e)\cos(b^e)\ddot{y}(5760\sin^4(b^e)}{240b^{e12}} \\ \quad + \frac{48b^{e7}(20 + b^{e5}(9\cos(2b^e) + \ddot{y}(25 + \ddot{y}(15 - b^{e4}(62\sin(2b^e) + b^e(\sin(4b^e) + \ddot{y}(120 - b^{e3}(22\cos(2b^e) + b^e(\cos(4b^e) + \ddot{y}(15 \end{cases}$$

$$I_{k^{04}}(b^e) = \frac{60b^{e2}(66\sin(2b^e) + b^e(7\sin(4b^e) + \ddot{y}(1440 - b^e\sin^2(b^e)(2\cos(2b^e) + b^e(7 + b^e(4320\sin^3(b^e)\cos(b^e)}{120b^{e9}}$$

$$I_{k^{02}k^{00}}(b^e) = \frac{16b^{e5}(12 + b^{e4}\sin(2b^e) + b^e(3 - b^{e3}(16\cos(2b^e) + b^e(\cos(4b^e) + \ddot{y}(49 + \ddot{y}(6 - b^{e2}(22\sin(2b^e) + b^e(3\sin(4b^e)}{12b^{e8}}$$

$$+ \frac{24b^e\sin^2(b^e)(7\cos(2b^e) + b^e(23 + \ddot{y}(288\sin^3(b^e)\cos(b^e)}{12b^{e8}},$$

$$I_{k^{00}2}(b^e) = \frac{b^{e3}(\cos(2b^e) + b^e(5 + b^e(2 - b^{e2}\sin(b^e)\cos^3(b^e)\ddot{y}(4 - b^e\sin^2(b^e)(\cos(2b^e) + b^e(3 + b^e(8\sin^3(b^e)\cos(b^e)}{2(b^e)^7},$$

$$I_{k^{02}}(b^e) = \frac{2(b^{e4}\ddot{y}(3 - b^{e2}(\sin^2(b^e)\ddot{y}(6 - b^e\sin(2b^e)(2 + b^e(18\sin^2(b^e)}{3b^{e5}},$$

$$I_{k^{00}}(b^e) = \frac{b^e(2 - b^e(\sin(2b^e) + b^e\ddot{y}(4\sin^2(b^e)}{b^{e4}},$$

$$I_{d^{02}}(b^e) = \frac{b^{e4}(3 + b^{e2}\sin^2(b^e)(6 - b^e\sin(2b^e)\ddot{y}(12\sin^2(b^e)}{3b^{e6}},$$

$$I_{ze}(b^e) = \frac{\ddot{y}(16 - b^{e4}\sin(b^e)(6 - b^{e3}(\cos(3b^e)\ddot{y}(11\cos(b^e)(2 + b^e(2 - b^{e2}(87\sin(b^e)\ddot{y}(33\sin(3b^e)}{24b^{e8}}$$

$$+ \frac{264b^e\sin^2(b^e)\cos(b^e)\ddot{y}(192\sin^3(b^e)}{24b^{e8}},$$

$$I_{ck^{02}}(b^e) = \ddot{y}\frac{\sin(b^e)(\ddot{y}(2 - b^{e3}(2 + b^{e2}\sin(2b^e)(4 - b^e(\cos(2b^e)(2 + b^e\ddot{y}(6\sin(2b^e)}{2b^{e5}},$$

$$I_{ck^{00}}(b^e) = \frac{\cos(b^e)(2 - b^{e2}(2 + b^e\ddot{y}(4\sin^2(b^e)}{2b^{e4}},$$

$$I_c(b^e) = \frac{2\sin(b^e)}{b^e}. \qquad (A.3)$$

References

Abaqus, 2012. Abaqus 6.12 Documentation.

Cochelin, B., Damil, N., Potier-Ferry, M., 2007. Méthode Asymptotique Numérique. Hermes Sciences.

COMSOL Multiphysics, 2011. User's Guide v4.2.

Dinis, P.B., Camotim, D., Silvestre, N., 2009. Gbt formulation to analyse the buckling behavior of thin-walled members with arbitrarily branched open cross-sections. Thin-Walled Struct. 47, 583–600.

Euler, L., 1744. Methodus inveniendi lineas curvas maximi minimive proprietate gaudentes, vol. 24.

Gonçalves, P.D., Camotim, D., 2009. Gbt formulation to analyse the first-order and buckling behaviour of thin-walled members with arbitrary cross-sections. Thin-Walled Struct. 47, 583–600.

Goss, V., 2009. The history of the planar elastica: insights into mechanics and scientific method. Sci. Educ. 18, 1057–1082.

Guinot, F., Bourgeois, S., Cochelin, B., Blanchard, L., 2012. A planar rod model with flexible thin-walled cross-sections. application to the folding of tape springs. Int. J. Solids Struct. 49 (1), 73–86.

Hoffait, S., Bruls, O., Granville, D., Cugnon, F., Kerschen, G., 2009. Dynamic analysis of the self-locking phenomenon in tape-spring hinges. Acta Astronaut. 66 (7–8),

Karkar, S., Arquier, R., Cochelin, B., Vergez, C., Lazarus, A., Thomas, O., 2010. MANLAB 2.0, An Interactive continuation software.

Schardt, R.P., 1994. Generalized beam theory – an adequate method for coupled stability problem. Thin-Walled Struct. 19, 161–180.

Seffen, K., Pellegrino, S., 1999. Deployment dynamics of tape springs. Proc. R. Soc. A 455, 1003–1048.

Seffen, K., You, Z., Pellegrino, S., 2000. Folding and deployment of curved tape springs. Int. J. Mech. Sci. 42 (10), 2055–2073.

Silvestre, N., 2007. Generalised beam theory to analyse the buckling behaviour of circular cylindrical shells and tubes. Thin-Walled Struct. 45 (2), 185–198.

Silvestre, N., Camotim, D., Silva, N., 2011. Generalized beam theory revisited: from the kinematical assumptions to the deformation mode determination. Int. J. Struct. Stab. Dyn. 11 (5), 969–997.

Vlassov, B., 1962. Pièces longues en voiles minces. Eyrolles, Paris.

Walker, S., Aglietti, G., 2007. A study of tape spring fold curvature for space deployable structures. Proc. Inst. Mech. Eng. Part G (J. Aerosp. Eng.) 221 (G3), 313–325.